HELIX-I: AN ISOLATED ROTOR, HOVER PERFORMANCE PREDICTION METHODOLOGY

Marvin A. Moulton[1], Mahendra J. Bhagwat[2], and Francis X. Caradonna[3]

[1] US Army AMRDEC, Aviation Engineering Directorate
Redstone Arsenal, AL, United States
e-mail: marvin.moulton@us.army.mil

[2] ELORET Corp.
Moffett Field, CA, United States
e-mail: bhagwat@merlin.arc.nasa.gov

[3] US Army AMRDEC, Aeroflightdynamics Directorate
Moffett Field, CA, United States
e-mail: caradonna@merlin.arc.nasa.gov

Keywords: hover performance, vorticity embedding, rotorcraft

Abstract: The first generation vorticity embedding code, called HELIX-I, is capable of accurately predicting the hover performance of realistic rotor configurations with reasonable speed. However, the solution process of this first implementation did not possess the robustness that one requires in an engineering method. With the goal of producing an accurate and robust analysis, a thorough re-examination and modification of the total solution process has resulted in a second generation embedding hover analysis, called HELIX-IA (HELIX-I, Army version). This paper will review the various solution stage modifications which were required to satisfy robustness requirements. Comparison with available data verifies the accuracy of these modifications. As a result of the modifications, the original HELIX-I has evolved into a robust tool capable of performing routine engineering analysis.

1 INTRODUCTION

Prediction of hover performance is a perennial problem of rotorcraft aeromechanics — a problem made particularly difficult by the high sensitivity of inflow and induced-power to the wake geometry and strength distribution. Therefore, hover performance analysis capabilities are primarily limited by our ability to accurately predict important details of the rotor wake system. An example of a hovering rotor wake is shown in Fig. 1, where the rotor tip vortices can be seen to follow helicoidal paths below the rotor disk plane. Although the hovering wake geometry is relatively simple, its influence on rotor blade loading and performance is not easy to predict because of the extreme sensitivity of loading to wake location. Much code development has been devoted to hover performance predictions over the past decades. The problem, however, is far from satisfactorily solved. This is because no method yet combines the dependability, generality, operational simplicity and accuracy required of an engineering method.

Hover performance prediction tools range from Lagrangian methods (both prescribed and free-wake, respectively) to Euler/Navier-Stokes Computational Fluid Dynamics (CFD) methods. Lagrangian methods are the current engineering method-of-choice for hover wake prediction because of their speed. However, these methods suffer from the manifold occurrence of wake instabilities and the complex logic and procedures required to avoid these instabilities. The most widely used methods are those in which wake trajectories are not free, but specified from experimentally derived data sets. This approach obviates troublesome convergence and robustness problems. Of course, such methods suffer from accuracy difficulties, because of inevitable limitations of the available experimental wake data sets. Nevertheless, many users would rather correct for accuracy deficiencies rather than tolerate computational robustness problems.

Figure 1: Example of tip vortex geometry of a hovering helicopter rotor.

CFD hover research has proceeded with a view to obviating this complexity arising from wake instabilities in Lagrangian solution techniques. It is certainly an attractive idea to overcome the difficulties resulting from wake convection and instabilities by simply solving the basic conservation laws. However, such CFD computations are complicated by the persistent problem of minimizing numerical dissipation. To overcome this problem, most present CFD methods require very dense grids and massive parallel computations. Even if such computations maintained adequate wake resolution, they are not compatible with everyday engineering needs.

In response to the need for an improved engineering tool, Steinhoff & Ramachandran [1] devised a unique methodology called "vorticity embedding". The key to this approach is decomposition of the velocity field into irrotational and rotational components. The irrotational velocity field is determined by an Eulerian potential flow solver. The rotational velocity field (or vortical velocity field) results from the shed wake and is determined from a vortex-lattice, free-wake. The crux of the method, described in the next section, is the procedure by which the vortical velocity field is impressed upon the background Eulerian field grid. An advantage of this method is that the induced velocity is not computed using the Biot-Savart law, but rather through the potential solution. Therefore, the computational effort is only slightly affected by increasing the number of panels that represent the wake.

Since the vorticity embedding method is a Lagrangian method, it suffers from much of the same known stability/robustness problems as standard vortex-lattice methods. In addition, the method exhibits some of its own instability mechanisms because of the necessity to simultanously converge the Lagrangian wake integration and the Eulerian potential flow solution. The first generation vorticity embedding code, called HELIX-I, is capable of accurately predicting the hover performance of realistic rotor configurations with reasonable speed [2]. However, the solution process of this first implementation did not possess the robustness that one requires in an engineering method. This paper outlines a thorough re-examination and modification of the total solution process which has resulted in a second generation vorticity embedding hover analysis, called HELIX-IA (HELIX-I, Army version). The basic method is briefly reviewed followed by a more in-depth discussion of the various solution stage modifications, which were required to improve robustness.

2 METHODOLOGY

In this section, a general description of vorticity embedding, as originally implemented in the HELIX-I code, is outlined. In the course of enhancing this original methodology, various techniques within the iterative process have been modified to improve both stability and accuracy of the overall technique. Since these modifications are extensive, they are only summarized in this section. Detailed descriptions of these improvements can be found in Refs. 3, 4, 5, 6 and 7.

2.1 HELIX-I Vorticity Embedding

The original HELIX-I code is a full potential flow solver that provides an inherently coupled solution of blade loading with a force-free vortex-lattice wake by means of vorticity embedding. The potential solution with an embedded wake structure obviates the need for large number of Biot-Savart induced velocity calculations for the wake induced velocity field, which allows for significantly detailed modeling of the wake structure without the associated increase in computational costs. In traditional potential flow CFD implementations , the shed circulation is expressed as a potential discontinuity surface that coincides with a grid plane. With such an implementation, the only way to computationally describe a freely evolving wake is to employ a dynamically evolving grid. However, the distortions in the typical rotor wake sheets are such that a wake-tracking grid would soon become topologically impractical.

In vorticity embedding, the wake vorticity is "embedded" into the potential flow by virtue of a convecting vortical velocity field, $\vec{q}_v$. The total velocity field is composed of three parts: the free stream, potential (irrotational), and vortical (rotational) velocity, i.e.,

$$\vec{V} = \vec{V}_\infty + \nabla\phi + \vec{q}_v \tag{1}$$

where $\vec{V}_\infty$ is the unperturbed free stream (in this case, the rotor rotational velocity), the potential part, $\nabla\phi$ contains the velocity induced by blade(s) and wake, and all vortical velocity components are contained in the term, $\vec{q}_v$, which defines the wake structure. When this velocity decomposition is inserted in the mass conservation equation, the result

$$\nabla\cdot\rho\vec{V} = 0 \quad \Rightarrow \quad \nabla\cdot(\rho\nabla\phi) = -\nabla\cdot(\rho\vec{q}_v) \tag{2}$$

is simply the standard steady (compressible) full-potential equation with the addition of a vortical forcing function or a source term. For compressible problems, the density, ρ, is computed using the Bernoulli equation,

$$\rho = \left[1 + \frac{\gamma-1}{2}M_\infty^2\left(\vec{V}_\infty^2 - \vec{V}^2\right)\right]^{\frac{1}{\gamma-1}}. \tag{3}$$

The vortical velocity field represents a typical singularity-surface model of the wake sheet(s). It is relatively straightforward to determine the wake geometry by using a Lagrangian convection method where the wake sheet is comprised of discrete markers [8]. These markers represent a zero-thickness circulatory wake sheet emanating from the rotor trailing edge. The surface defined by these markers is the basis for construction of the vortical velocity field. The potential solver provides both the blade lift distribution and the convection velocities for the Lagrangian marker integration. The HELIX-I solution process then iterates between these two parts: the non-homogeneous potential equation and the Lagrangian wake trajectory integrations, see Fig. 2.

Figure 3 shows a typical cylindrical grid used for HELIX-I solutions. Each radial grid plane is a two dimensional H-grid around the blade section. These sectional H-grids are then stacked radially to form the complete rotor H-H grid. The H-grid topology results in a double line in the grid, where the upper and lower surface grids coalesce (except on the blade surface). The grid extends azimuthally $2\pi/N_b$ around a reference blade, and periodicity conditions at the azimuthal boundaries capture effects of the other blades. The example shown in Fig. 3 is for the four-bladed UH-60A rotor, so the grid extends 90 degree in azimuth. The grids are concentrated

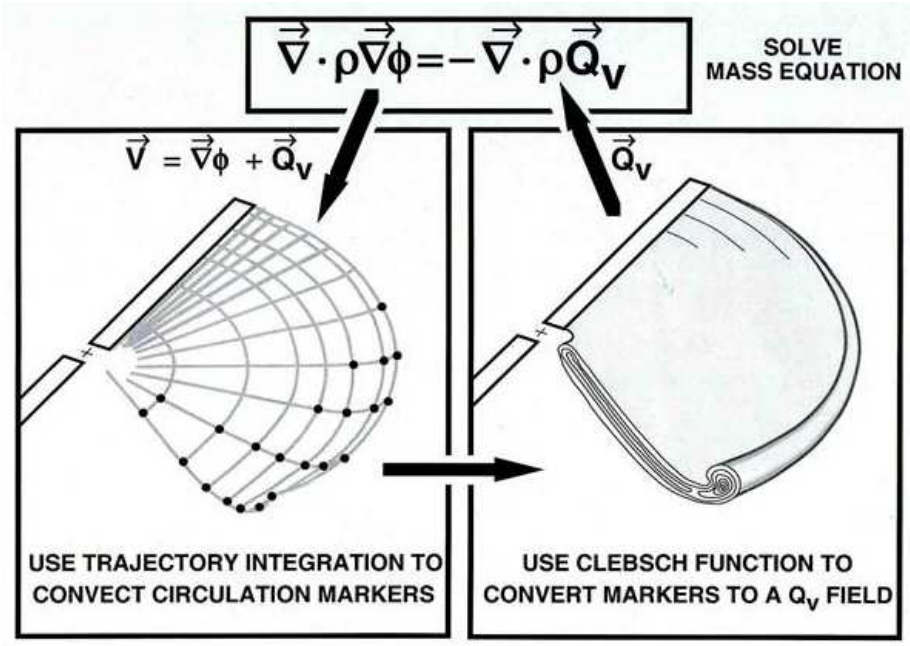

Figure 2: An iterative solution method is devised wherein the wake is first described as a singularity sheet, then converted to vortical velocity field, which becomes a forcing function to the potential equation

azimuthally and axially near the blade to improve blade loading calculations, and also radially in the tip region to better capture the tip vortex location.

The original HELIX-I code was successfully applied to hover and axial flight performance predictions of several well-known rotor configurations [2]. The induced lift and drag are directly calculated from the potential flow solution by performing pressure integration over the blade surface. The profile drag is calculated using a non-interacting Nash-McDonald boundary layer model. Although the performance predictions agreed well with experimental data, the solutions were sometimes susceptible to wake instabilities, and often required user intervention. Moreover, the predicted wake geometries did not always follow well-known empirically observed trends.

The following sections describe the three integral parts of the free-wake solution process: the wake integration algorithm, the potential solver and the vortical velocity construction. Each section highlights the enhancements from the original implementation. A description of a new "lifting-surface" mode is also included. Incorporation of these enhancements into the original code has resulted in the second generation code called HELIX-IA.

2.2 Wake Integration

The aforementioned deleterious traits associated with the original HELIX-I code appeared to be associated with the explicit treatment of the wake trajectory integration. Therefore, initial enhancement efforts focused on improving the wake trajectory integration algorithm. The original code employed a first-order, backward Euler trajectory integration, which is known to admit a number of instabilities. The enhanced code utilizes a second-order, predictor-corrector method, similar to the University of Maryland Free-Wake [8].

To assess the effectiveness of this modification, UH-60A hover performance predictions for both versions are compared in Fig. 4. Both predictions compare fairly well with the experimental Figure-of-Merit (FM) data reported in Ref. 2, see Fig. 4(a). However, notice that the modified code results appear to follow the trend of the data better than those resulting from the original

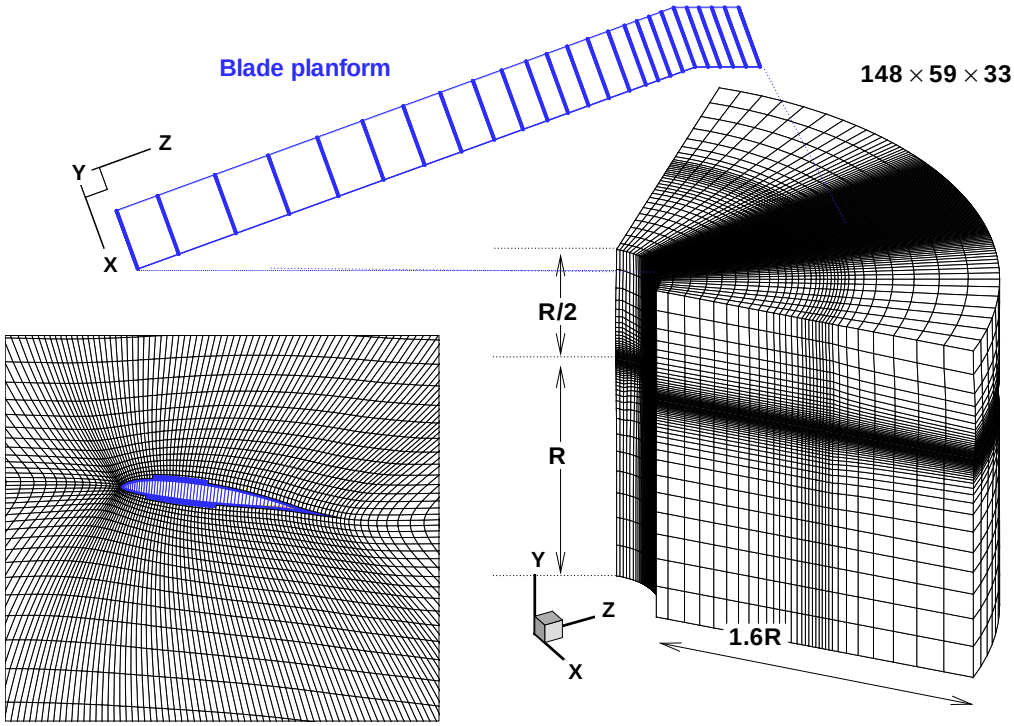

Figure 3: Typical HELIX-I *grid geometry for a four-bladed rotor with 148×59×33 grid cells in the azimuthal, axial and radial directions, respectively. A constant radius section shows the H-grid surrounding a blade cross-section. Grid is stretched near the rotor blade in axial and azimuthal directions, and near the blade tip in the radial direction.*

code. To better understand these trends consider the definition of Figure-of-Merit

$$\mathrm{FM} = \frac{C_T^{3/4}}{C_Q} \tag{4}$$

where C_T and C_Q are the rotor thrust and torque coefficients, respectively. The torque includes contributions from both the induced drag as well as the profile drag. Since HELIX-I is an inviscid analysis, the profile drag is obtained from an auxilary source (in these cases a Nash-McDonald boundary layer approximation). Perhaps, a better assessment of the wake integration enhancement is to compare trends for the ideal FM, which does not include the profile drag.

Figure 4(b) shows the trends comparison for the ideal FM. Since the ideal FM is not measurable, the figure includes the trend based on combined blade element/momentum theory (BE/MT). It is noteworthy that the original HELIX-I predictions do not follow the essentially linear decreasing trend with increasing rotor thrust. However, the modified code with improved wake integration does show the expected trend. Even though the agreement in absolute values is not great, these encouraging early results propelled further work on the HELIX-I code leading to development of enhancements to the potential solver and vortical velocity construction.

2.3 Potential Solver

The original HELIX-I code employed a semi-implicit, finite-volume, potential solver. In various test problems, it was determined that the convergence/stability of the solver was excessively grid dependent which necessitated restrictive grid quality control. Therefore, the original algo-

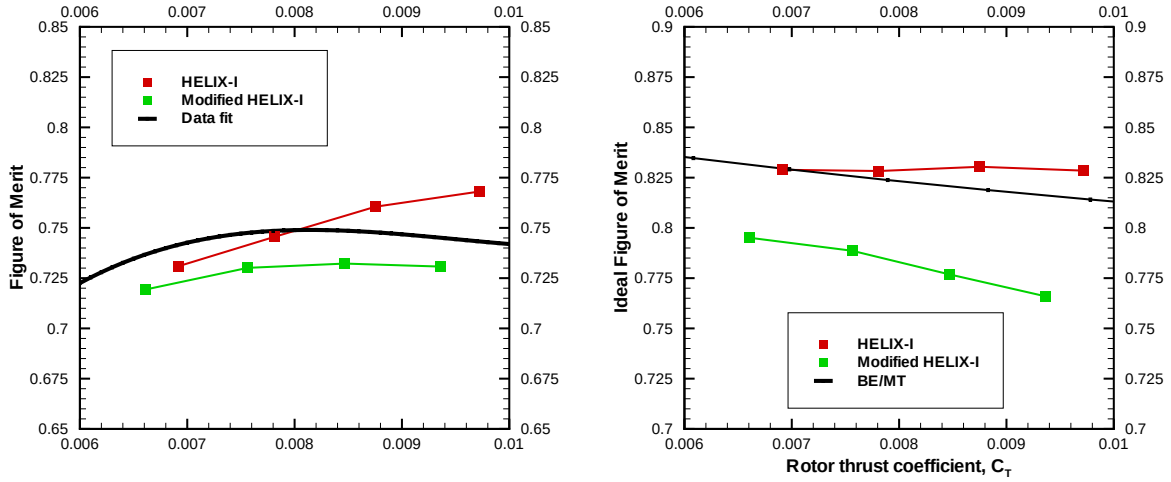

(a) Figure-of-Merit (b) Ideal Figure-of-Merit

Figure 4: Example showing effect of initial modifications to the wake trajectory integration algorithm.

rithm was subsequently replaced with a fully implicit solver based on the AF-1 algorithm [9]. This solver and its convergence characteristics, as implemented in the current version of the code, are described in Refs. 3 and 4. The finite volume formulation necessitates an additional grid coupling term in order to eliminate the problem of "odd-even decoupling." The enhanced algorithm takes advantage of these compensation terms by setting their coefficients to increase the order of accuracy and convergence rate of the solver with no change in the computational stencil.

To demonstrate the effectiveness of the solver enhancements (in particular, the inclusion of compensation terms), an ordered approach was utilized to solve a hierarchy of problems beginning with the most simple and ultimately working up to a full hover problem [3]. The most simple flow problem was "no flow at all", a seemingly ridiculous computation performed by bisecting an entire computational grid with an unvarying circulation sheet. Because the circulation sheet has no variation and no edges, there is no vortex-induced flow. Computing this was not trivial, however, and revealed a number of solver problems associated with vortical velocity construction The next level of difficulty is to put an edge on the sheet. When this edge extends entirely across the computational region in a straight line it represents a 2D vortex or a line vortex, with its well-known analytic solution. Making the sheet edge a circle represents the flow about a vortex ring, whose solution is also known. The final specified-geometry sheet would be for a spiral sheet extending from a leading-edge line (a "lifting-line") to a grid boundary. This is the classical prescribed wake problem, which can be built up to a free wake problem by allowing the strength and location of the vortex sheets to vary. Another simple test problem was set-up to calculate the 2D flow around an airfoil section or a flat-plate lifting-surface to examine loading calculations. Convergence trends for these test problems are summarized in Fig. 5.

Notice that the solver without the compensation terms showed significantly slower convergence for all test problems. Also, the convergence progressively deteriorated as the complexity of the flow field increased — compare the vortex ring and helical wake sheet in Fig. 5(a). With the addition of the compensation term, however, the convergence rate was the same for a given grid for all test problems. This is an encouraging result because it shows that the potential flow convergence does not depend on the complexity of the wake structure in the vorticity embedding procedure.

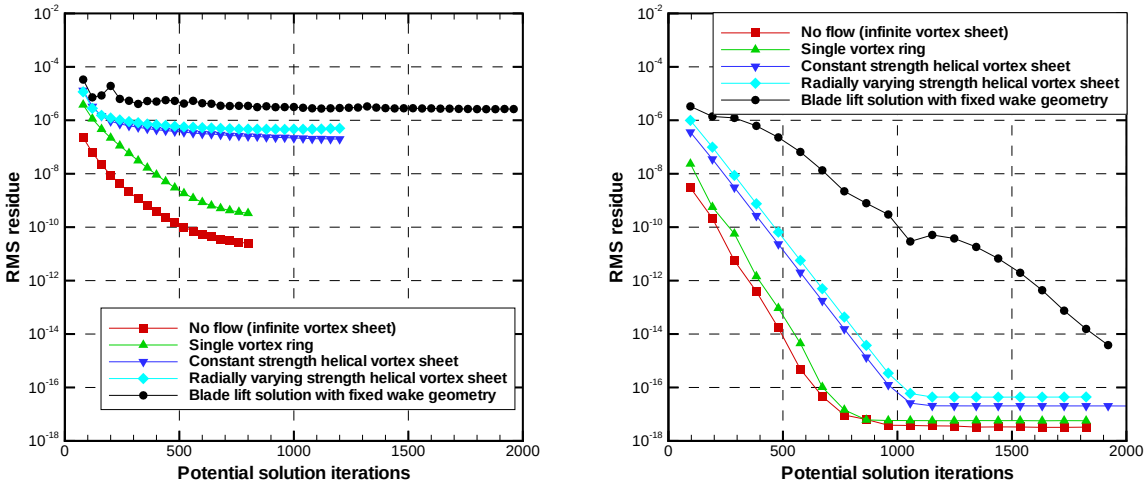

(a) Convergence without the compensation terms

(b) Convergence with 2nd-order compensation terms

Figure 5: Effect of compensation terms on the potential solver convergence for a hierarchy of test problems.

2.4 Vortical Velocity Construction

The real key to the success of the vorticity embedding lies in the vortical velocity field, $\vec{q}_v$, which is constructed to emulate the wake singularity surface(s). It must be noted that this field is *not* the induced velocity of the wake, but only a representation of the wake structure. It is a "carrier field," that contains sheet circulation distribution in a form compatible with the potential equation. In order to represent the wake sheet(s) on a discrete Eulerian grid used for the potential solver, it is necessary to represent it as a field quantity. Therefore, it must have a finite thickness. Ideally, the vorticity should be constrained within an infinitesimally small distance around the wake sheet, since it is devised to represent a surface singularity. However, the discrete nature of the solution means that the vorticity can at best be restricted to a region of 2 grid intervals around the wake sheet. This is the objective of the new vortical velocity formulation.

There are many ways in which the vortical velocity field could be constructed. Circulation conservation requires only that the line integral of velocity normal to, and passing through the vortical velocity field (and the underlying wake marker sheet) must equal the local sheet circulation. An efficient algebraic vortical velocity construction process has previously been described in Ref. 4. This formulation satisfies the circulation conservation requirement, but does not restrict the vorticity to a thin region. Typically the vortical velocity field layer thickness was of the order of 8 to 10 grid intervals, and the vorticity resulting from this field was also spread over that distance. The original implementation using this formulation occasionally displayed anomalies that were traced to elongated tip vortex structures, which were about 2 grid intervals wide (as the $\vec{q}_v$ field was "cut-off" at the edge of the sheet) and about 8 grid intervals high (the $\vec{q}_v$ field thickness). This was corrected by a special treatment of the edge of the wake sheet described in Ref. 5, where the vorticity at the very tip of the vortical velocity field was "reshaped" so as to compress it within 2 grid intervals. While this approach produced reasonably robust solutions, it was eventually discovered that deficiencies remained and were manifest as excessive grid sensitivity of the solution.

This grid sensitivity problem led to the development of a new vortical velocity formulation. The original formulation of Refs. 4 and 5 was essentially an extension of a formula for a vortex sheet of constant strength. The new formulation is more general and includes effect of variation of circulation strength along the wake sheet, in the form of an additional tangential velocity component. In principle, this can be considered as a generalization of the special tip "reshaping"

treatment discussed in Ref. 5. However, the formulation is much simpler, and is given succinctly as

$$\vec{q}_v = \underbrace{\Gamma_{\text{avg}} \nabla\lambda}_{\text{normal to sheet}} - \underbrace{\left[\int_{S_n}^{\infty} \nabla\lambda\right]_{\text{avg}} \nabla\Gamma}_{\text{tangential to sheet}} \tag{5}$$

where Γ is the sheet circulation (may be a function of distance along the sheet) and λ is the Clebsch function, a normal distribution function

$$\lambda(S_n, a) = \begin{cases} -\frac{1}{2} & S_n < -a \\ \frac{1}{2}\sin\left(\frac{\pi}{2}\frac{S_n}{a}\right) & -a \le S_n \le a \\ +\frac{1}{2} & S_n > a \end{cases} \tag{6}$$

where S_n is the normal distance from the wake sheet, and a is the specified thickness. Note that the first term in Eq. 5 is normal to the sheet because λ varies only along a direction normal to the sheet, as given by Eq. 6. The original formulation of Refs. 4 and 5 included only this first term in Eq. 5. This term is sufficient to ensure that the circulation in the flowfield around the wake sheet is conserved, independent of the grid distribution and the thickness, a.

The second term of Eq. 5 is tangential to the wake sheet because of the gradient of the sheet circulation. This term compresses the vorticity represented by the vortical velocity field into a thin layer (of the order of the grid interval) independent of the thickness, a. The circulation strength drops to zero at the sheet edge giving a large circulation gradient and a correspondingly large second term in Eq. 5. The behavior of this term at the tip is essentially the same as that of the tip "reshaping" process in Ref. 5. Therefore, this new formulation can be viewed as a generalization of that process.

To demonstrate the modeling aspects of this new formulation, Fig. 6 shows a cross-section of the shed rotor wake in a $r-z$ plane just behind the blade. For clarity, only the portion of the wake emanating from the preceding blade is shown in the figure. Overlaid on the vortical velocity field (denoted by vectors) are the Lagrangian markers and contours of the resultant vorticity field. In Fig. 6(a), only the first term of Eq. 5 is used to construct the vortical velocity field. Because of the large thickness of the vortical velocity field layer, the vorticity is also spread over a large thickness. Therefore, the contours are nearly imperceptible, except close to the tip. Furthermore, the tip vortex is seen to be stretched into an oblong region, which was the motivation for the previous "tip reshaping" formulation.

Figure 6(b) demonstrates the effect of including the second "compression" term in Eq. 5. In this case also, the vortical velocity remains spread over a large region, as in Fig. 6(a). Yet, the vorticity is confined to a thin layer that is clearly dicernable from root to tip, centered around the underlying wake marker sheet.

To illustrate the grid sensitivity of the "reshaping" formulation, Fig. 7 shows UH-60A hover performance predictions using a baseline grid with two grid variations. The first grid variation utilizes the same number of grid points as the baseline grid with a small change in the radial spacing along the blade span. The second grid variation has 25% more grid points in the radial and axial directions. The variation in Figure-of-Merit is large considering the relatively small variations in the grid distributions.

To demonstrate the effectiveness of the new formulation with its accompanying vorticity compression, UH-60A hover performance predictions were repeated using the same baseline grid and its varations. Clearly, as shown in Fig. 8, the compression of the vortical wake thickness greatly reduces the sensitivity of the performance predictions to small variations in the grid. We suspect these results are somewhat indicative of what can be expected to occur in any CFD computation where the wake sheets can possibly diffuse and become too thick or completely disappear. Of course, this is easily avoided in the present method because the potential flow solution is inherently free of diffusion.

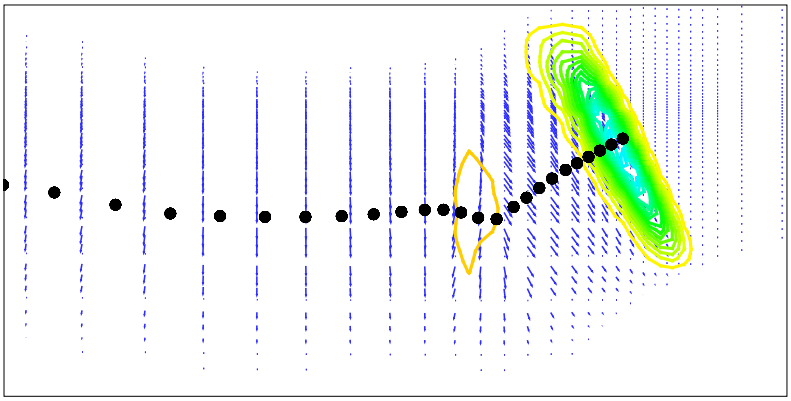

(a) Vorticity contours with only the normal $\vec{q}_v$ component

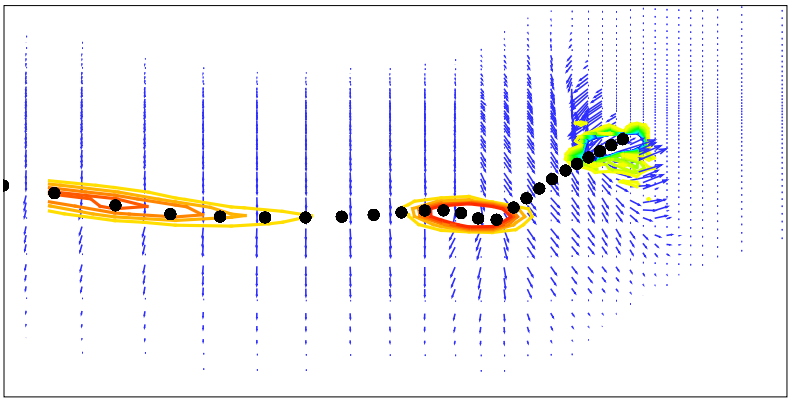

(b) Vorticity contours with the tangential $\vec{q}_v$ component included

Figure 6: Vorticity "compression" achieved by the new vortical velocity formulation.

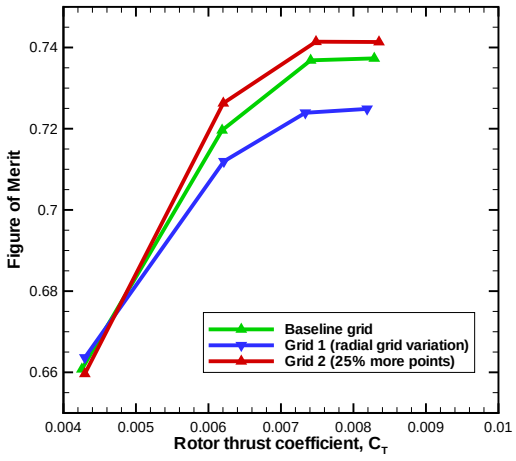

Figure 7: Variation of performance predictions using the previous "tip reshaping" formulation of Ref. 5.

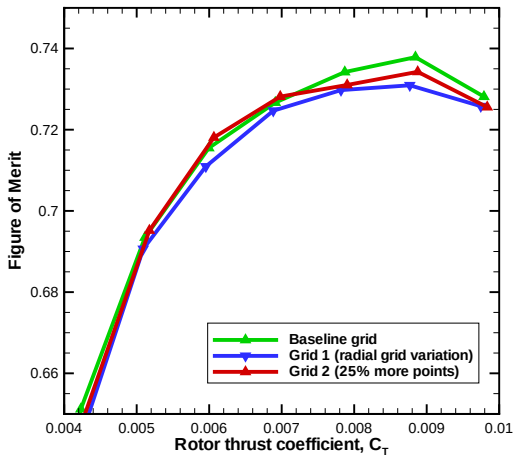

Figure 8: Variation of performance predictions using the vortical velocity formulation.

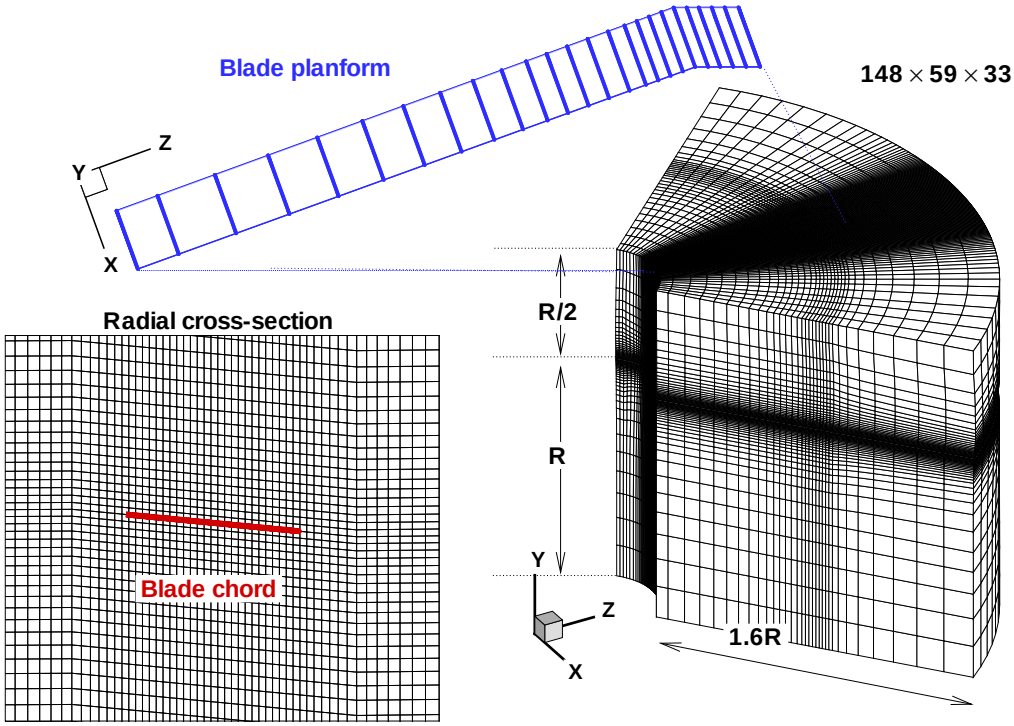

Figure 9: Typical HELIX-IA *grid geometry for a four-bladed rotor with 148×59×33 grid cells in the azimuthal, axial and radial directions, respectively. A constant radius section shows the H-grid surrounding a flat lifting-surface representing the blade section.*

2.5 Grid Effects

In spite of the above improvements, it was still extremely difficult to generate a surface-conforming grid that would resolve both the local blade flow and the wake flow. The primary difficulty seems to arise from the blade leading edge region where the H-topology is singular. A further complication, although not as severe as the leading edge, arises from the cylindrical pie-shape of the grid, which requires significant grid stretching near the blade tip region because of the increased streamwise arc-length. Since the H-grid is ideal for wake convection, this topology is retained. However, to alleviate the problems associated with surface-conforming H-grids a "lifting-surface" approach that utilizes an auxiliary method to predict profile power requirements was employed to resolve the local blade flow.

Figure 9 shows a typical cylindrical grid now used for HELIX-IA solution. Each radial grid plane is a two dimensional H-grid around the blade section. These sectional H-grids are then stacked radially to form the complete rotor H-H grid. The H-grid topology results in a double line in the grid, where the upper and lower surface grids coalesce. The grid extends azimuthally $2\pi/N_b$ around a reference blade, and periodicity conditions at the azimuthal boundaries capture effects of the other blades. The example shown in Fig. 9 is for the four-bladed UH-60A rotor, so the grid extends 90 degree in azimuth. The grids are concentrated azimuthally and axially near the blade to improve blade loading calculations, and also radially in the tip region to better capture the tip vortex location. The 'lifting-surface' mode of HELIX-IA represents the blade by a flat lifting surface along the blade chord as shown in Fig. 9. It should be noted that the use of a lifting surface grid is not inherent to the method. Rather, good results obtained with this simple grid make it difficult to justify a more detailed grid. Moreover, when a hybrid solution is required, a surface-conforming grid is unnecessary.

The flat-plate airfoil solution is numerically equivalent to thin airfoil theory. Note that such a

thin airfoil representation cannot compute chordwise force and, hence, drag; thin airfoil theory gives identically zero drag. In the case of blade surface-conforming grids, sectional forces can be easily calculated by pressure integration. Pressure integration over the flat-plate would, however, result in a net force normal to the chord axis regardless of the incident flow angle. Instead, the magnitude of the sectional lift can be obtained from the bound circulation using the Kutta-Joukowski theorem. However, the direction of the lift vector is harder to find because the effective inflow is unknown.

A simple approach to estimate the inflow distribution is to find the an effective angle of attack from the bound circulation through Kutta-Joukowski theorem and thin airfoil theory, i.e.,

$$\left.\begin{aligned} L &= \rho V_\infty \Gamma_b \\ C_l &= \frac{2\pi}{\sqrt{1-M^2}}\alpha \end{aligned}\right\} \Rightarrow \alpha_{\text{eff,2D}} = \frac{\Gamma_b\sqrt{1-M^2}}{\pi V_\infty c}. \tag{7}$$

A better approach to estimate the local inflow is using the Weissinger-L model, which is a panel method with a single chord-wise panel. The blade bound circulation is assumed to be at the quarter chord and the flow tangency condition is satisfied at a control point located at three-quarter chords. As shown in Ref. 5, the sectional lift and (induced) drag coefficient are then given by

$$C_l = \frac{2\Gamma}{V_\infty c}\cos\left(\theta - \beta\alpha_{\text{eff,3D}}\right) \tag{8}$$

$$C_d = \frac{2\Gamma}{V_\infty c}\sin\left(\theta - \beta\alpha_{\text{eff,3D}}\right) \tag{9}$$

where $\alpha_{\text{eff,3D}}$ is the effective angle of attack and β is the Prandtl-Glauert factor. Performance calculations can now be performed with the lifting-surface model using the estimated angle of attack given by the Weissinger-L model and the normal force coefficient given by the Kutta-Joukowski theorem.

It should be noted that an even simpler blade representation, referred to as the "lifting-line" mode, has previously been developed wherein the leading edge of the wake sheet represents the blade. For this model, the blade bound circulation must be specified from external information. This mode of operation, initially developed for debugging purposes, is ideally suited for a hybrid computation process where the bound circulation is derived from an inner Reynolds Averaged Navier-Stokes (RANS) solution.

3 RESULTS

Good validations has been obtained using model UH-60A rotor data of Lorber *et al.* [10]. This particular data is remarkable for its completeness, containing performance, detailed surface pressure and wake trajectory data. The importance of having all these data is that comparison with integrated performance alone leaves room for many counteracting errors. CFD (in addition to many other methods) can show very good performance prediction without correctly predicting the vortex passage location below the

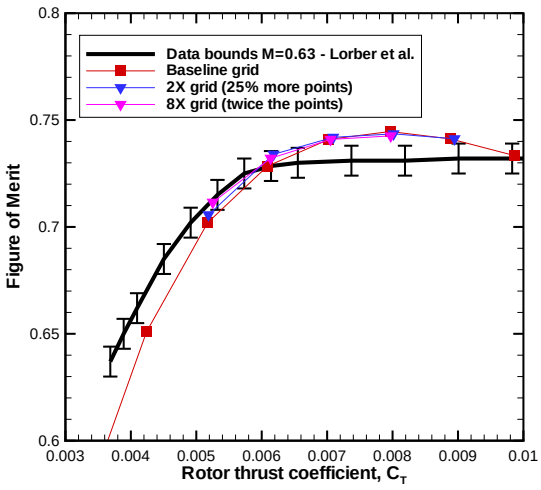

Figure 10: Comparison of predicted isolated rotor hover performance with data (Model UH-60A, $M_{\text{tip}} = 0.63$).

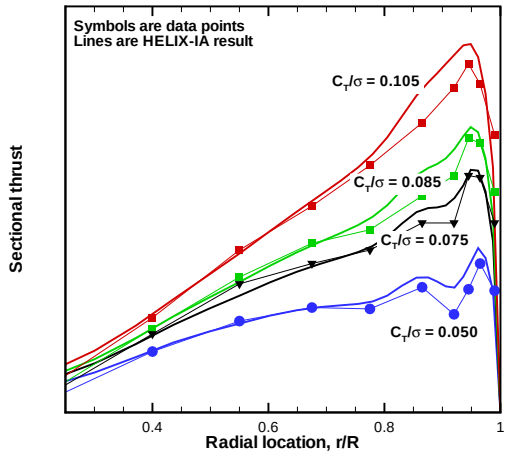

Figure 11: Comparison of predicted spanwise loading with data (Model UH-60A rotor, $M_{\text{tip}} = 0.63$).

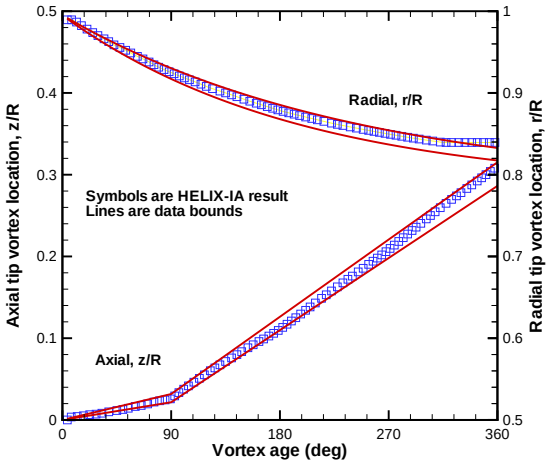

Figure 12: Tip vortex trajectories compared with experimentally determined error bands (Model UH-60A rotor, $C_T/\sigma \approx 0.085$, $M_{\text{tip}} = 0.63$).

blade, e.g., Ref. 11. Only when wake trajectory and radial lift distribution are well predicted can one have reasonable confidence in performance (FM vs C_T) comparisons. Figure 10 shows a comparison of computed and measured performance in terms of Figure-of-Merit as a function of rotor thrust coefficient. HELIX-IA solutions with three grids are shown. The baseline grid is $126 \times 107 \times 33$ in the azimuthal, vertical and spanwise direction with 25 points on the blade surface in both the chordwise and spanwise directions. The $2\times$ grid used 25% more points in each direction, while the $8\times$ grid used twice the number of points in each direction. Clearly, the performance computations are nearly grid independent and give good confidence in the predictive capabilities of the HELIX-IA code.

Although the integrated performance predictions using HELIX-IA compare very well with data, it is the additional comparison of wake trajectory and radial lift distribution (Figs. 11 and 12) that demonstrates its fundamental soundness. Figure 11 shows a comparison of computed and measured sectional thrust for four collective pitch settings. Figure 12 shows a comparison of tip vortex radial and axial trajectories for one representative case at a collective pitch setting of 10 degrees that corresponds to $C_T/\sigma \approx 0.085$. The good agreement between predictions and data for all these basic features of hovering rotor flowfield — wake, loading and performance — attests to the validity of the vorticity embedding method as an engineering analysis tool.

To further validate the methodology, HELIX-IAwas exercised to predict the performance for a tapered-tip rotor (a tip replacement for the previously mentioned UH-60A model rotor, see Ref. 10). This rotor has a 3:1 taper near the blade tip (linearly from $0.823r/R$). The grid for computing such a blade was rather large (almost six times) as compared to the typical grid described earlier. Note that this increased grid size was not meant for solution resolution, but was dictated by potential solver stability considerations, as described in Ref. 5. only 25 points were used on the blade surface in both chordwise and spanwise directions. The resulting grid was about 2.5 million nodes and required over 6 hours of CPU time per case.

The performance polar for this rotor operating at a tip Mach number of 0.55 is shown in Fig. 13. At lower thrust levels, the predictions compare very well with the measured data. However, at higher thrusts, the predictions lack the characteristic drop in Figure-of-Merit seen in data because of tip stall [10]. Although the profile drag obtained from C81 table look-up models some increase in power because of stall, the resulting loss of lift is not captured by the potential flow solution. This can also be seen in the spanwise loading comparisons shown in Fig. 14, which compares the measured and computed sectional thrust distribution. At lower thrusts, the

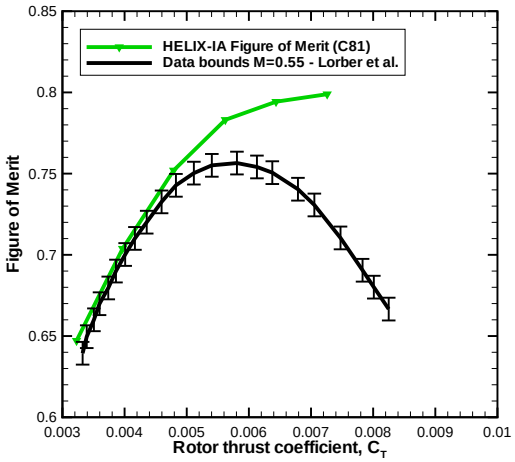

Figure 13: Comparison of predicted spanwise loading with data (3:1 tapered tip rotor, $M_{\text{tip}} = 0.55$).

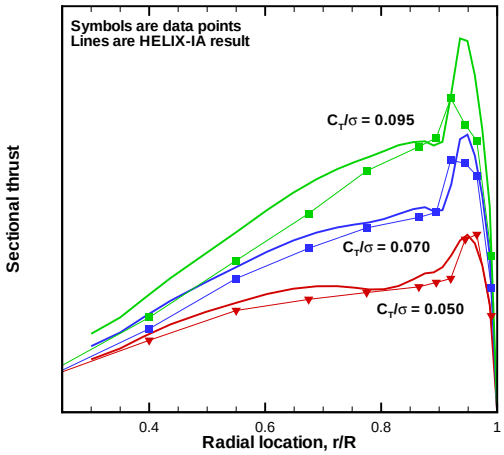

Figure 14: Comparison of predicted spanwise loading with data (3:1 tapered tip rotor, $M_{\text{tip}} = 0.55$).

predictions and data show a good agreement, whereas at higher thrust the agreement gets worse, especially in the tip region where the potential flow computations are not applicable due to the presence of stall. In such cases, a hybrid solution methodology must be employed with an inner RANS blade loading solution capable of capturing separated flows and stall.

The final data set presented for validating the HELIX-IA solutions is obtained from of an interesting rotor test performed in 1937 by Knight & Hefner [12]. This test measured performance of four different rotor configurations, having 2, 3, 4 and 5 blades. These blades were untwisted and used a NACA0015 airfoil section. The reason for the lack of blade twist was to permit the testing of a simple scaling law based on solidity that would reduce the data for these different number of blades onto a single curve. We use a similar scaling, using blade number instead of solidity, that gives the following functional relations

$$\frac{C_T}{N_b^2} = f\left(\frac{\theta}{N_b}\right) \tag{10}$$

$$\frac{C'_Q}{N_b^3} = g\left(\frac{\theta}{N_b}\right). \tag{11}$$

The HELIX-IA code has been employed to show that the rotor thrust and induced torque (i.e., torque without profile drag) do indeed scale as predicted. Comparison of HELIX-IA rotor thrust predictions is shown in Fig. 15, which gives the thrust as a function of the collective pitch in the K-H similarity form, Eq. 10. This figure shows that for all rotor configurations and for both test and computation, all values of C_T/N_b^2 lie on a single line and the test and computational values are reasonably close. Because the profile power does not scale with solidity or blade-number, Knight & Hefner proposed a modified torque coefficient, C'_Q, which does not include the zero-lift profile drag (C_{d_0}) contribution. When the torque results are plotted in the K-H similarity form as the modified torque coefficient against θ/N_b, the different rotors again fall on a single curve as seen Fig. 16, and compare very well with the experimental data.

Figure 17 shows comparisons of FM versus scaled collective pitch angle for the four rotor configurations, and it is seen that they are all well predicted. Since the profile power does not scale with blade-number, the FM curves do not coalesce together. Now consider Fig. 18 which plots the ideal (induced) Figure-of-Merit as a function of the scaled collective pitch. Ideal Figure-of-Merit is defined as the ratio of ideal power to the induced power, without including the profile drag. It is seen that now all curves collapse fairly closely onto a single curve. This demonstrates

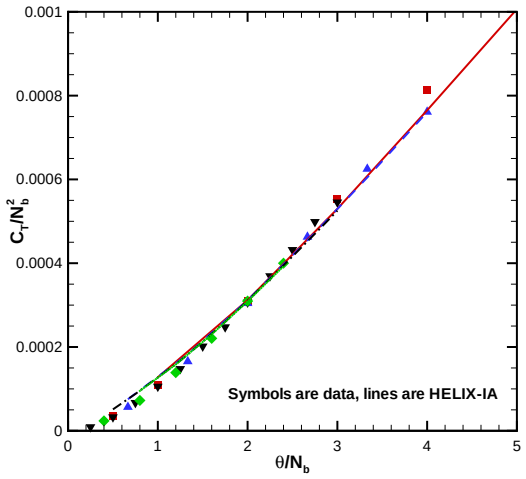

Figure 15: Variation of rotor thrust with collective pitch setting for the Knight & Hefner rotors.

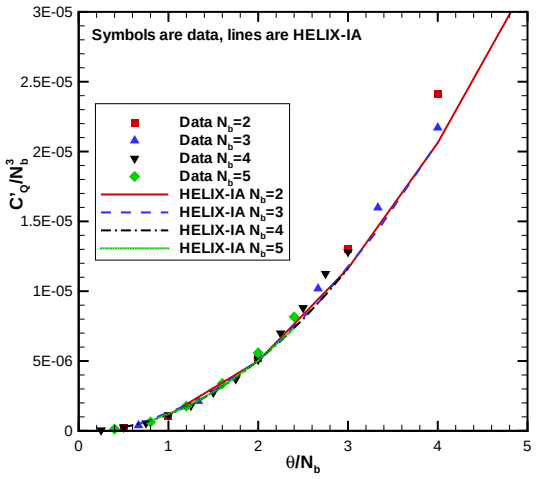

Figure 16: Variation of rotor induced torque (modified) with collective pitch setting for the Knight & Hefner rotors.

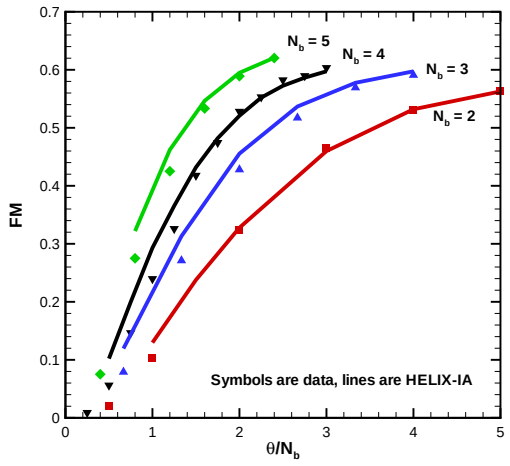

Figure 17: Comparison of the Figure-of-Merit variation for the Knight & Hefner rotors.

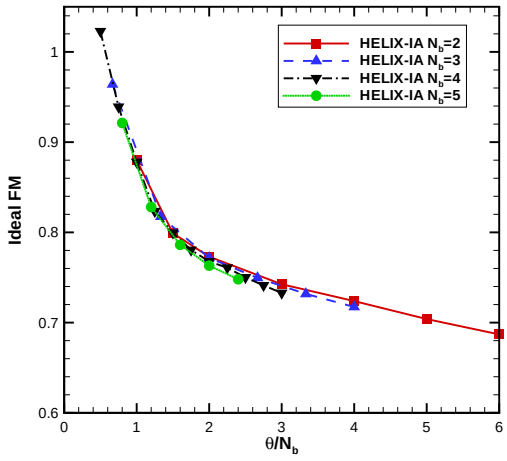

Figure 18: Comparison of the ideal Figure-of-Merit variation for the Knight & Hefner rotors.

not only the efficacy of a little-known scaling, but also that of the vorticity embedding method, as implemented in HELIX-IA, is consistent with the flow equations that constitute the basis of the scaling.

4 SUMMARY & CONCLUSIONS

This paper has presented a new implementation of the vorticity-embedding method, called HELIX-IA, for the computation of free-wake, rotor hover performance. The combination of its robustness, versatility, modeling accuracy, and speed make it a credible engineering tool for rapid investigation of blade geometry design space. Confidence in HELIX-IAis demonstrated by good comparisons with available data and the general robustness of the method.

The single most important validation data base is the model UH-60A data since it includes extensive data for the wake and loading. Experience has shown that without the ability to accurately predict these, there is no basis for trust in the performance prediction. Throughout the development cycle of the various HELIX-IA variants, comparison with the UH-60A data has

been the main yardstick of progress. We have shown that the HELIX-IA compares reasonably well with the wake, loading and performance data for the UH-60A blade. In addition, we have shown that this comparison is relatively insensitive to grid variations. Both the Figure-of-Merit and the ideal Figure-of-Merit (which is not directly measurable) were found to be the most sensitive indicators of progress. Good comparisons of Figure-of-Merit were not usually obtained until wake geometry and loading were predicted consistently well. When this occurred it was always found that the ideal Figure-of-Merit had a characteristic decreasing trend with thrust.

Another valuable set of data (and analysis) is now almost 70 years old. This is from the multi-blade-number rotor test of Knight & Hefner (K-H). In the presentation of their data, K-H employ a surprisingly little-known similarity scaling, which reduces the results of all the different blade numbers onto a single curve for both thrust and a properly defined torque, an astonishing simplification. Many of the K-H configurations and test conditions have been modeled with HELIX-IA, and the comparison with data is good. Figure-of-Merit is one of those quantities that does not reduce to a single curve since the profile power does not scale. However, the ideal Figure-of-Merit, containing no profile power, does reduce closely to a single curve. When computed with HELIX-IA this curve has the characteristic shape discussed previously. The K-H scaling is very important in the evaluation of CFD hover methods as it provides one simple curve for ideal Figure-of-Merit that infers the general ability of a method to accurately compute the wake, blade loading and induced power which is what we expect in an engineering method.

Finally, we have seen limitations of the present method for configurations where stall can occur. This shows the need for a future inner viscous blade solver that is coupled to the HELIX-IA code which is an ideal wake solver to use for this purpose. Previous attempts to hybridize (utilize an inner viscous solver to compute blade loads) the HELIX-IA code have relied upon the original HELIX-I technology. Now, given the accuracy and robustness of HELIX-IA, future variations to the hybrid code can concentrate on enhancements that improve resolution of the viscous flow.

5 ACKNOWLEDGMENTS

The present paper represents over twenty years of development, beginning with an ARO (Army Research Office) sponsored Ph.D. thesis at the University of Tennessee Space Institute (UTSI). In the subsequent years, development has been supported by the Army Aeroflightdynamics Directorate (AFDD) at Moffett Field, California. Other support for this work has come from the U.S. Army Aviation and Missile Research, Development & Engineering Center at Huntsville and, most recently, this work has been supported by the ONR Naval Air Vehicle Technology Discovery & Invention program (N0001406WX20241). The authors are also thankful for the many technical suggestions and criticism provided by Sikorsky Aircraft over the years.

6 REFERENCES

[1] Steinhoff, J. S. and Ramachandran, K., "Free Wake Analysis of Helicopter Rotor Blades in Hover Using a Finite Volume Technique," Report DAAG29-84-K-0019, U. S. Army Research Office, Research Triangle Park, NC, October 1988.

[2] Ramachandran, K., Owen, S. J., Caradonna, F. X., and Moffitt, R. C., "Hover Performance Prediction Using CFD," American Helicopter Society 50^{th} Annual National Forum, Vol. II, Washington, DC, May 11–13, 1994, pp. 1259–1273.

[3] Bhagwat, M. J., Moulton, M. A., and Caradonna, F. X., "Recent Advances in the Embedded-Wake Approach to Hover Performance Prediction," AHS 4^{th} Decennial Specialists' Conference on Aeromechanics, San Francisco, CA, January 2004.

[4] Bhagwat, M. J., Moulton, M. A., and Caradonna, F. X., "Development of a New Potential Flow based Hover Performance Prediction Method," AIAA 43^{rd} Aerospace Sciences Meeting, Reno, NV, January 2005.

[5] Bhagwat, M. J., Moulton, M. A., and Caradonna, F. X., "Development of a CFD-based Hover Performance Prediction Tool for Engineering Analysis," AHS 61^{st} Annual National Forum, Grapevine, TX, June 2005.

[6] Bhagwat, M. J., Moulton, M. A., and Caradonna, F. X., "Development and Application of a CFD-based Engineering Analysis of Hover Performance," AHS 62^{nd} Annual National Forum, Phoenix, AZ, May 9-11 2006.

[7] Bhagwat, M. J., Moulton, M. A., and Caradonna, F. X., "Hybrid CFD for Rotor Hover Performance Prediction," AIAA 24^{th} Applied Aerodynamics Conference, San Francisco, CA, June 2006.

[8] Bhagwat, M. J. and Leishman, J. G., "Stability, Consistency and Convergence of Time-Marching Free-Vortex Rotor Wake Algorithms," *Journal of the American Helicopter Society*, Vol. 46, (1), January 2001, pp. 59–71.

[9] Ballhaus, W. F., Jameson, A., and Albert, J., "Implicit Approximate-Factorization Schemes for Steady Transonic Flow Problems," *AIAA Journal*, Vol. 16, (6), June 1978, pp. 573–579.

[10] Lorber, P. F., Stauter, R. C., Pollack, M. J., and Landgrebe, A. J., "A Comprehensive Hover Test of the Airloads and Airflow of an Extensively Instrumented Model Helicopter Rotor," Vol. 1-5, USAAVSCOM TR-D-16 (A-E), October 1991.

[11] Wake, B. E. and Baeder, J. D., "Evaluation of a Navier-Stokes Analysis Method for Hover Performance Prediction," *Journal of the American Helicopter Society*, Vol. 41, (1), January 1996.

[12] Knight, M. and Hefner, R. A., "Static Thrust Analysis of The Lifting Airscrew," Technical Report TN 626, NACA, December 1937.